Nano Research

ISSN 1998-0124 CN 11-5974/O4
https://doi.org/10.26599/NR.2026.94908383

Research Article

Tunable microwave absorption driven by electrochemically air-breathing

Xinyu Xie[1,2], Yufeng Wu[1,2,3], Yunzhi Li[1,2], Anqi Li[1,2], Jiaoyang Gong[1,2], Chang Li[1,2], Zhuting Zhang[2], Hsiang-shun Chang[2], Yan Feng[2], Tanyi Wang[1,2], Peng Du[4], Hehe Wei[2], Jianchun Xu[1], Yunjian Guo[1], Kai Huang[1](✉), Ming Lei[1,5], Ke Bi[1](✉), Hui Wu[2,3](✉)

[1] State Key Laboratory of Information Photonics and Optical Communications, School of Physical Science and Technology, Beijing University of Posts and Telecommunications, Beijing 100876, China

[2] State Key Laboratory of New Ceramic Materials, School of Materials Science and Engineering, Tsinghua University, Beijing 100084, China

[3] Wuzhen Laboratory, Tongxiang 314500, China

[4] Zhejiang Key Laboratory for Island Green Energy and New Materials, Institute of Electrochemistry, School of Materials Science and Engineering, Taizhou University, Taizhou 318000, China

[5] State Key Laboratory of Information Photonics and Optical Communications & School of Integrated Circuits, Beijing University of Posts and Telecommunications, Beijing 100876, China

Nano Res., **Just Accepted Manuscript** • https://doi.org/10.26599/NR.2026.94908383
https://www.sciopen.com/journal/1998-0124 on Dec. 29, 2025

Tunable microwave absorption driven by electrochemically air-breathing

TABLE OF CONTENTS (TOC)

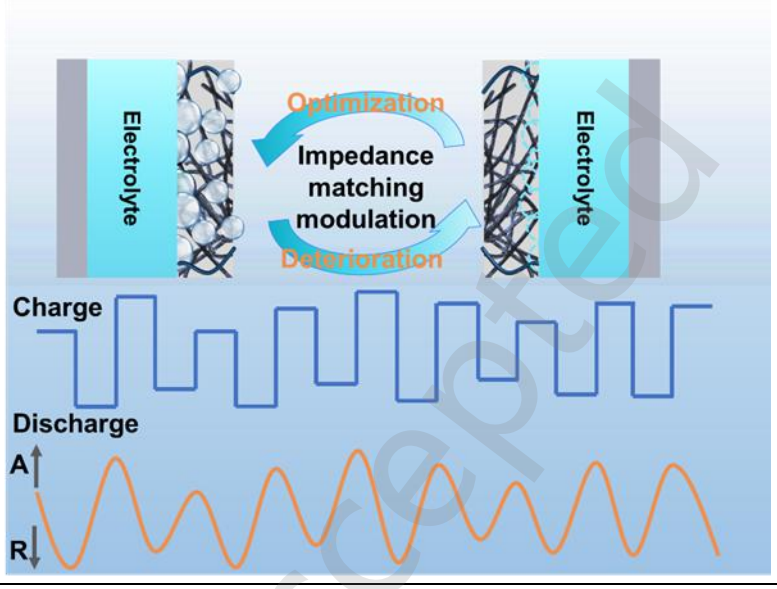

In this work, we demonstrated an intelligent microwave modulation driven by electrochemical impedance-matching interface.

Nano Research

Open Access

Research Article

Tunable microwave absorption driven by electrochemically air-breathing

Xinyu Xie[1,2], Yufeng Wu[1,2,3], Yunzhi Li[1,2], Anqi Li[1,2], Jiaoyang Gong[1,2], Chang Li[1,2], Zhuting Zhang[2], Hsiang-shun Chang[2], Yan Feng[2], Tanyi Wang[1,2], Peng Du[4], Hehe Wei[2], Jianchun Xu[1], Yunjian Guo[1], Kai Huang[1]✉, Ming Lei[1,5], Ke Bi[1]✉, and Hui Wu[2,3]✉

[1] *State Key Laboratory of Information Photonics and Optical Communications, School of Physical Science and Technology, Beijing University of Posts and Telecommunications, Beijing100876, China*

[2] *State Key Laboratory of New Ceramic Materials, School of Materials Science and Engineering, Tsinghua University, Beijing 100084, PR China*

[3] *Wuzhen Laboratory, Tongxiang 314500, China*

[4] *Zhejiang Key Laboratory for Island Green Energy and New Materials, Institute of Electrochemistry, School of Materials Science and Engineering, Taizhou University, Taizhou 318000, China*

[5] *State Key Laboratory of Information Photonics and Optical Communications & School of Integrated Circuits, Beijing University of Posts and Telecommunications, Beijing 100876, China*

Received: 3 November 2025; **Revised:** 23 December 2025; **Accepted:** 29 December 2025

✉Address correspondence to Kai Huang, huang-kai@bupt.edu.cn; Ke Bi, bike@bupt.edu.cn; Hui Wu, huiwu@tsinghua.edu.cn

Cite this article: *Nano Research*, **2026**, *19*, 94908383. https://doi.org/10.26599/NR.2026.94908383

ABSTRACT: With the rapid development of information technology, electromagnetic protection and compatibility issues have an indispensable role in daily life, social development and military applications of national defense. However, the current electromagnetic absorption materials are limited in that they can only offer a fixed level of absorption loss, making them challenging to adapt to complex application environments. This study integrates electrochemical devices with conventional multilayer wave-absorbing structures, leveraging multilayer interfacial coupling effects and dynamic impedance matching during device operation to achieve tunable wave-absorption performance. The system demonstrates a maximum modulation efficiency of 15 dB while retaining its regulatory capability after 200 bending cycles. By incorporating zinc-air battery modules into multilayer wave-absorbing materials, this work overcomes the limitations of traditional tunable absorbers that rely on mechanical deformation or thermally induced phase transitions for performance modulation. The proposed design not only simplifies modulation mechanisms but also significantly reduces energy consumption during absorption adjustment and enhances response speed, offering a novel paradigm for tunable wave-absorbing materials.

KEYWORDS: tunable microwave absorption, electrochemically modulation, impedance matching

Introduction

The rapid advancement of information technology, particularly the ongoing transition from 5G to 6G in communication systems, has resulted in increasingly complex electromagnetic environments [1]. Such complexity poses significant challenges to electromagnetic compatibility (EMC), making effective protection against EM interference a critical research priority.

Unlike conventional EM shielding materials that primarily rely on reflection mechanisms [2], electromagnetic wave-absorbing materials (EMA) dissipate incident EM energy through dielectric, magnetic, or conductive losses, converting it into thermal or other energy forms [3]. These materials have drawn extensive attention for their ability to fundamentally suppress secondary EM pollution caused by reflection [4]. Recent studies have further emphasized that absorption-dominated electromagnetic attenuation should be achieved through synergistic loss mechanisms and optimized impedance matching, rather than relying on reflection suppression alone [5]. Current EMA research has mainly focused on achieving thin profiles, broad bandwidth, lightweight design, and strong absorption [6]. Although carbon-based materials, dielectric ceramics, and magnetic composites partially meet these requirements, their absorption remains static—limiting adaptability to dynamic EM environments encountered in defense, aerospace, and advanced electronic systems [7,8]. It has been increasingly recognized that dynamic regulation of conductive networks and interfacial polarization states is essential for maintaining efficient electromagnetic absorption under complex and evolving EM conditions [9]. Therefore, developing dynamically tunable EMA technology and device has become an urgent demand.

To realize dynamically tunable absorbers, diverse modulation strategies have been explored. For example, Chen et al. designed a VO_2 nanoparticle–incorporated aerogel that enables reversible switching of absorption via thermally induced phase transitions, achieving an effective absorption bandwidth (ΔEAB) of 7.27 GHz and a reflection loss (ΔRL) change of 49 dB [10]. However, its reliance on thermal stimuli limits real-time response and application versatility [11]. Wang et al. further developed a compressible aerogel whose EM parameters are tuned by mechanical compression, continuously adjusting ΔEAB up to 13.4 GHz with a modulation depth of 35 dB [12]. Nevertheless, the mechanical control mechanism complicates integration. Alternatively, Li et al. proposed a transistor-based metasurface absorber capable of voltage-controlled impedance modulation, allowing dynamic absorption adjustment between 20%–80% [13]. Yet, its bulky configuration hinders miniaturization and large-scale deployment [14,15]. In contrast, electrochemical modulation provides a promising pathway toward compact, energy-efficient, and highly integrable tunable absorbers. Han et al. recently demonstrated an electrochemically controlled MXene-based EM shielding device, achieving a ~7 dB modulation at selected frequencies and validating the feasibility of active electrochemical EM regulation [17]. Future research should focus on advancing electrochemical modulation pathways to realize higher modulation depth and broadband tunability in electromagnetic absorbers.

Figure 1. Schematic illustration of the mechanism of electrochemically-driving tunable microwave absorption device.

Herein, we introduced a multilayer wave-absorbing device modulated by electrochemical reactions, composed of impedance matching layer, absorption layer, and reflection layer (Fig. 1) [18]. Through systematic in situ characterization, we confirmed that gas generation and consumption at the incident interface play a key role in regulating absorption efficiency. By coupling electrochemical reactions with dynamic impedance matching, tunable wave-absorption performance is achieved. The multilayer absorber exhibits dynamic electrochemical behavior at the incident interface, where *in-situ* oxygen generation and consumption directly regulate the impedance state of the matching layer. During discharge, oxygen consumption leads to impedance mismatch with air, increasing electromagnetic reflection and weakening absorption. In contrast, oxygen generation during charging improves impedance matching, allowing electromagnetic waves to penetrate into the multilayer structure, where multiple internal reflections enhance energy dissipation. The dynamical impedance-tunable multilayer WAM enables precisely controllable electromagnetic response modulation due to its simplified fabrication process, low cost, and scalable production capability that integrates with structural design.

Result and Discussion

2.1. Preparation and performance of bi-functional catalyst

We adopted a stepwise synthesis protocol for the CoO_x@NMC composite via a two-step protocol comprising liquid-phase mechanochemical blending and subsequent flash joule thermal processing, as shown in Fig. S1 [19]. The nitrogen-doped mesoporous carbon (NMC) matrix, serving as the carbon-based support, was homogenously integrated with cobalt nitrate precursor ($Co(NO_3)_2{\cdot}6H_2O$) through combined mechanochemical effects and controlled solvent evaporation. The applied shear forces during grinding induced particle surface activation, facilitating intimate interfacial contact between components. During the followed rapid joule-heating treatment, a nitrogen-doped mesoporous carbon-supported clustered CoO_x composite catalyst was formed. Fig. S2 corroborates the morphological evolution through comparative SEM analysis, revealing the

well-ordered particle distribution and successful loading.

As shown in Fig. 2(a)-(c), the powder after thermal treatment exhibits a successfully optimized phase composition, allowing the oxidation to be combined with the NMC. This resulted in a higher electrochemically active surface area, along with the formation of bifunctional catalyst, thereby promoting accelerated interfacial charge transfer while enhancing the efficiency of electrochemical reaction kinetics. Fig. 2(a)-(b) displays the HRTEM image of CoO_x@NMC, showing a well-defined interface with lattice fringes of 2.46 Å ascribed to the (311) lattice plane of Co_3O_4 phase, demonstrating that $Co(NO_3)_2$ undergoes successful oxidation to Co_3O_4 during thermal treatment. Fig. 2c provides an additional analysis of the SAED pattern, where several bright diffraction rings correspond to the (400) and (311) planes of Co_3O_4, which are consistent with the HRTEM images.

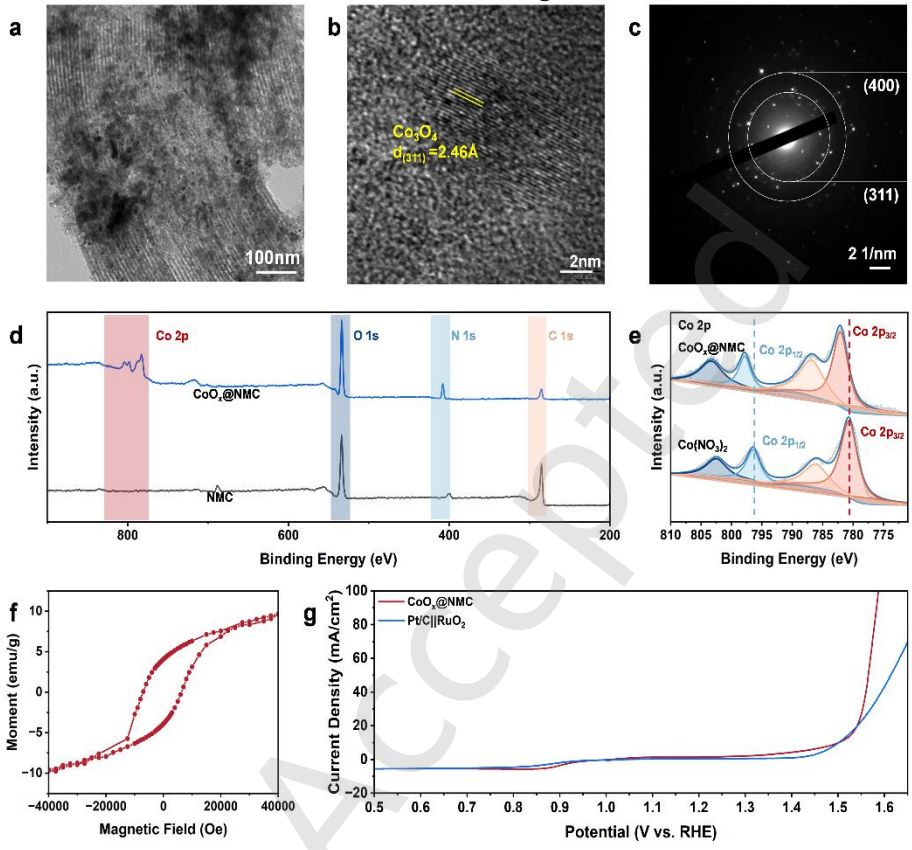

Figure 2. (a)-(b) The HRTEM images of synthesized CoO_x@NMC at different magnifications. (c) The SAED pattern of synthesized CoO_x@NMC. (d) The XPS survey of synthesized CoO_x@NMC. (e) The high-resolution Co 2p XPS spectra of CoO_x@NMC and pristine Co $(NO_3)_2$. (f) The M-H curve of CoO_x@NMC. (g) LSV curves for alkaline OER and ORR of synthesized CoO_x@NMC.

The crystalline phase evolution was systematically investigated through XRD pattern. As depicted in Fig. S3, all characteristic peaks corresponding to Co3O4 (JCPDS 42-1467) and CoO (JCPDS 48-1719) phases can be clearly identified for CoO_x@NMC, which is due to the controlled oxidation of Co species during the flash joule heating process under air atmosphere. Notably, the coexistence of Co_3O_4 and CoO phases combined with the NMC support suggests the formation of highly dispersed CoO_x domains with abundant interfacial contact, which is beneficial for subsequent electrocatalytic reactions.

Additionally, XPS analysis was conducted to investigate the electronic structure and chemical valence states of the CoO_x@NMC. Fig. 2(d) shows the XPS survey spectrum of the sample, revealing distinct photoelectron peaks corresponding to Co 2p, O 1s, C 1s, and N 1s orbitals. The presence of these characteristic peaks verifies the successful integration of $Co3O_4$ with the NMC framework. As evidenced by the Co 2p spectra in Fig. 2(e), the sample exhibits a positive binding energy shift compared to pristine Co $(NO_3)_2$, indicating electron loss from Co atoms and their transition to higher oxidation states. This valence state evolution confirms the successful transformation of the precursor into Co_3O_4 with enhanced oxygen evolution reaction (OER) activity. The observed peaks at 797.9 eV and 782.3 eV align with the characteristic electronic structure of Co^{3+}/Co^{2+} mixed-valence states in spinel Co_3O_4 [20]. As shown in Fig. S4(c), the deconvoluted O 1s spectra exhibit three peaks at 530.5, 532.5 and 533.3 eV, ascribing to the surface lattice oxygen (O_L), surface adsorbed hydroxyl groups (O_{OH}) and chemisorbed water (O_{MW}), respectively [21]. Obviously, the O_L component in CoO_x@NMC increases compared with $Co(NO_3)_2$, which also indicates a thermal transformation from $Co(NO_3)_2$ to CoO_x.

The above surface chemical state demonstrates that the valence of Co increased, revealing the formation of oxidation cobalt after thermal treatment under air atmosphere. Moreover, the nitrogen-doped mesoporous carbon framework provides strong electronic coupling with CoO_x and continuous conductive pathways, which facilitates fast electron transport and efficie nt electrolyte infiltration during electrochemical reactions. Furthermore,

as shown in Fig. 2(f), the pronounced magnetic hysteresis loop observed in the sample's M-H curve exhibits high coercivity and large remanent magnetization, characteristic of hard magnetic materials. These magnetic parameters align with the intrinsic properties of cobalt-based ferromagnetic systems, corroborating the successful formation of Co_3O_4 phase in the synthesized material.

The electrocatalytic performance of CoO_x/NMC electrocatalysts for both oxygen reduction (ORR) and evolution (OER) reactions was systematically investigated in 1 M KOH solution, confirming the enhanced ORR and OER activities of CoO_x@NMC. As depicted in Fig. 2(g), CoO_x@NMC sample demonstrates a similar ORR catalytic performance with Pt/C. Additionally, CoO_x@NMC sample demonstrates the most excellent OER catalytic performance with an overpotential of 357 mV to achieve the current density of 100 mA cm^{-2}, significantly lower than that of commercial RuO_2. Furthermore, CoO_x@NMC exhibits a considerably decreased Tafel slope of 60.3 mV dec-1, indicating accelerated OER kinetics and lower kinetic barriers at the Co active sites induced by atomic-scale dispersion and thermal activation. In contrast, the fitted Tafel slopes of commercial RuO_2 yield much higher values of 80.7 mV dec^{-1}, demonstrating the sluggish OER performance. These kinetic advantages originate from the atomic-scale dispersion of ultrafine CoO_x clusters within the nitrogen-doped mesoporous carbon matrix, which provides abundant accessible active sites, promotes efficient charge and ion transport, and facilitates rapid gas diffusion at the catalyst–electrolyte interface. The aforementioned high electrochemical performance facilitates the rapid generation of bubbles, thereby enhancing their capability to adjust impedance matching. This characteristic indicates a significant potential for applications in tunable electromagnetic absorption.

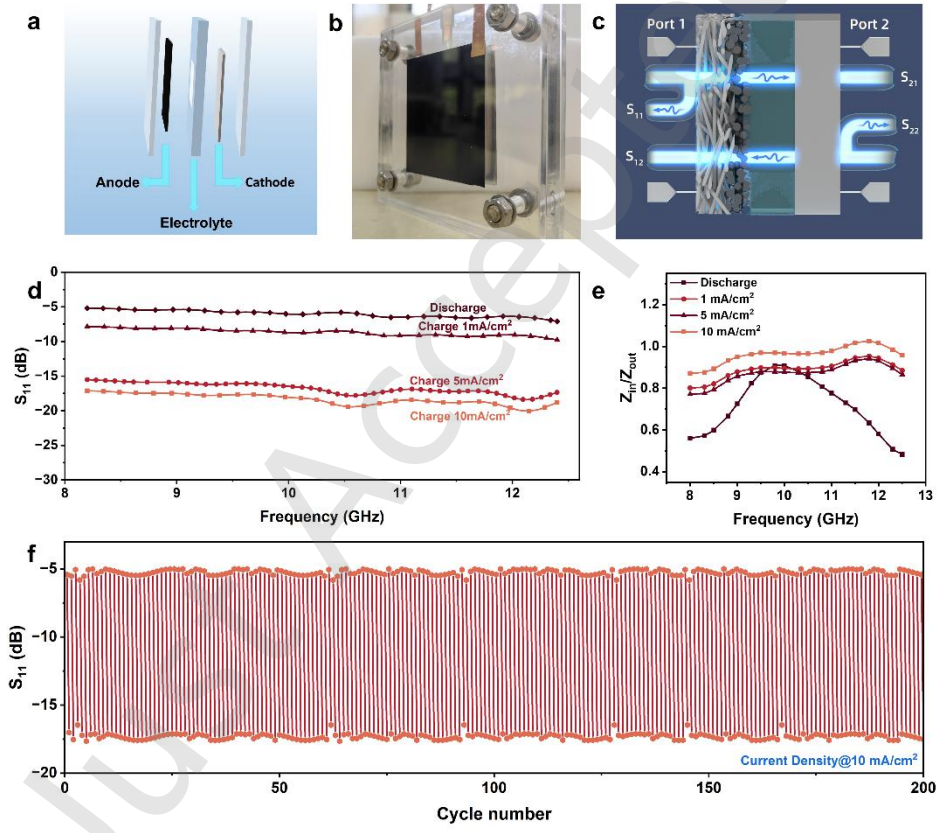

Figure 3. (a) Schematic illustration of the ZAB-based device. (b) The image of as-prepared ZAB-based device. (c) Schematic illustration of the waveguide transmission line method. (d) The S-parameters of the device under discharge and charging conditions at various current densities. (e) The impedance matching of the device under different conditions. (f) The durability test of the device.

2.2. Mechanism verification through ZAB-based device

To overcome the limitations of conventional tunable absorbers—particularly their dependence on mechanical deformation or thermally induced phase transitions for performance modulation—we developed a multilayer absorbing architecture that incorporates an integrated electrochemical system (Fig. 3(b)) [22]. This innovative design not only simplifies the modulation mechanism but also significantly reduces the energy consumption required for adjusting the absorbing performance while greatly enhancing the response speed of the device. These improvements provide new insights into the development of tunable absorbing materials. Firstly, the electrochemical characterization of the designed ZAB-based device was performed. In this study, commercial RuO_2+Pt/C catalysts were selected for the ZAB-based device due to their widespread application and demonstrated high efficiency in the catalytic field, aiming to establish a reliable benchmark for subsequent performance evaluations [24, 25]. Compared with devices utilizing commercial catalysts, those employing our homemade catalyst exhibited a significantly narrowed voltage window during both charge and discharge processes. Specifically, at a current density of 10 mA cm^{-2}, devices based on commercial catalysts operated over a broad

voltage range of approximately 0.7–2.7 V, whereas the device using CoO_x@NMC showed a much narrower and more stable voltage window of approximately 1.3–2.3 V, indicating improved reaction kinetics and reduced polarization (Fig. S5(a)), achieving an energy density of 18 mW/cm^2, which represents a 10 mW/cm^2 improvement over devices using commercial catalysts (Fig. S5 (b)). Furthermore, during stability tests, the device employing the self-prepared catalyst maintained excellent performance without significant degradation after continuous charge-discharge cycling for 12 hours (Fig. S5(c)).

Subsequently, following the establishment of the electrochemical performance foundation of the ZAB-based device, we carried out a systematic characterization and analysis of the device's electromagnetic wave absorption efficiency and its modulated performance. Due to the size constraints imposed by the device design, we utilized the waveguide transmission line method, as depicted in Fig. 3(c), to measure the S-parameters and electromagnetic properties of the device. In this study, the S-parameters were evaluated under discharging and charging conditions at various current densities. The findings revealed that the electromagnetic wave absorption efficiency of the device increased with higher current densities during charging, which is attributed to the bubble generation rate and intensity under different current densities. Additionally, as illustrated in Fig. 3(f), the study also confirmed that the device maintains its conditioning performance after multiple charge/discharge cycles. The results confirmed that the device maintained consistent regulation performance over 200 charge-discharge cycles (spanning 6 hours), thereby validating its stability. Despite the ZAB-based device designed in this study demonstrating a modulation effect on electromagnetic wave absorption efficiency across the frequency range of 12-18 GHz, with peak modulation efficiency reaching 12 dB, its thickness and reliance on an acrylic plate for support restrict the size of the effective reaction area. Furthermore, wave leakage occurred during the waveguide test, hindering its ability to achieve effective modulation across a broad frequency range. Therefore, we have implemented a flexible device configuration to address the aforementioned issues.

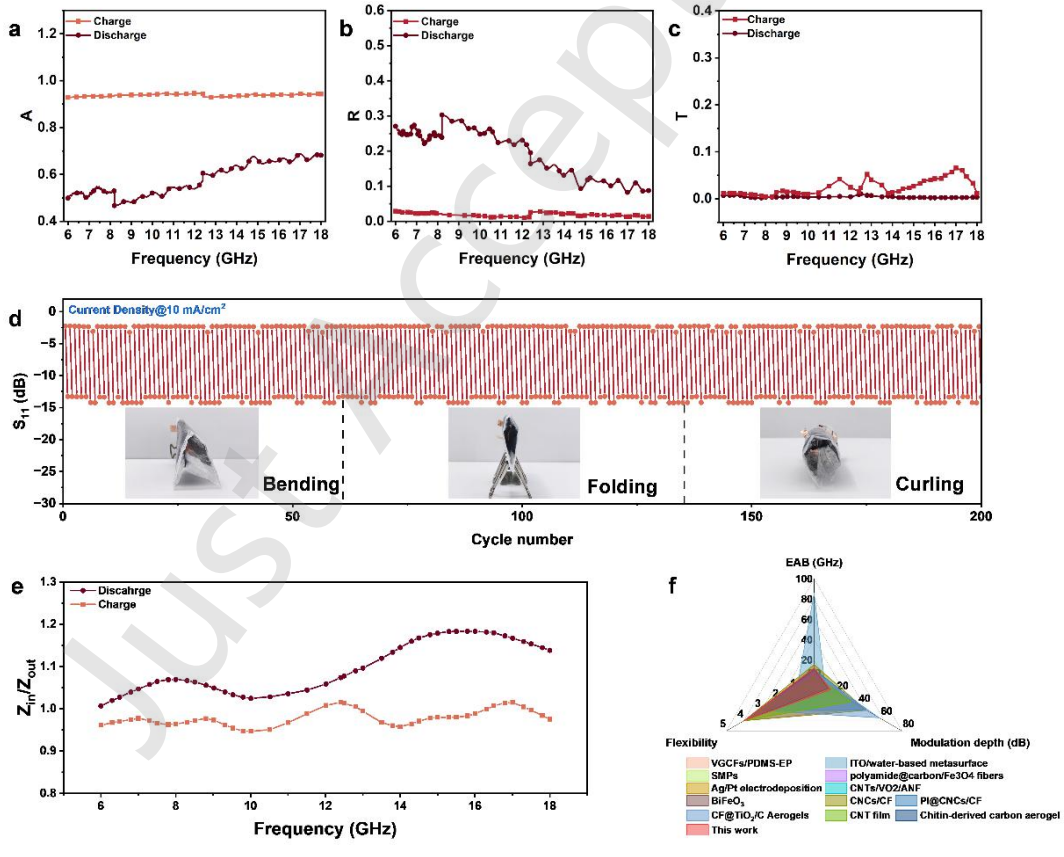

Figure 4. (a) The absorption parameters of the device under the condition of charging and discharging. (b) The reflection parameters of the device under the condition of charging and discharging. (c) The transparent parameters of the device under the condition of charging and discharging. (d) The durability test of the device after different bending conditions (bending, folding, curling). (e) The impedance matching of the device under the condition of charging and discharging. (f) The comprehensive comparison of the properties of different mechanisms.

2.3. Electrochemically modulated wave absorption with flexible device

Due to the aforementioned issues with ZAB-based device, this study designed flexible devices using hydrogel-based solid electrolytes [26], considering the potential requirements of wearable devices in practical application scenarios, possible deformation, and the need for large-scale devices [27].

First, compared to ZAB-based device, flexible device exhibits higher charge and discharge capacities while eliminating the necessity of separator plates required in ZAB-based device. The overall design relies on flexible hydrogel solid

electrolytes, which demonstrate significantly superior mechanical properties compared to ZAB-based device and can maintain excellent wave-absorbing modulation performance even after repeated bending. Furthermore, unlike ZAB-based device whose sizes are constrained by custom molds, flexible device can be scaled up with rational wiring, enhancing their practical applicability.

In the actual preparation process, this study developed a flexible device measuring 6 cm × 6 cm with a thickness of 3 mm (Fig. S7). Initially, we characterized the electrochemical performance of the device (Fig. S8). Compared to devices utilizing commercial catalysts, those employing our homemade catalyst exhibited a narrower voltage window during both charge and discharge cycles. This observation indicates that the self-synthesized CoO_x@NMC catalyst possesses a higher ion transfer number, resulting in enhanced energy efficiency and utilization rates for the prepared device. Simultaneously, we conducted stability tests on the fabricated device; experimental results demonstrated stable operation for 12 hours post-packaging without significant performance degradation, thereby confirming its stability. Following the removal of the acrylic plate support, the device thickness was significantly reduced, and the electromagnetic leakage observed during waveguide measurements was effectively suppressed compared with the ZAB-based device, which is attributed to the direct and conformal contact between the absorber and the waveguide surface.

Compared with the discharging state, the absorption coefficient A of our flexible device under the charging state increases by more than 50% over a broad frequency range of 6–18 GHz., while modulation of absorption efficiency reached an impressive maximum of 15 dB. Due to the inherent flexibility of the device developed in this study, we also characterized its stability following multiple bending, crimping, and folding cycles. As illustrated in Fig. 4(d), after undergoing 200 cycles of bending, folding, and curling, the modulation performance of the device exhibits no significant attenuation. This observation indicates that our flexible device possesses excellent mechanical properties and maintains its structural integrity despite repeated deformations. Unlike thermal or phase-change strategies that rely on slow, energy-intensive lattice or phase transformations, or mechanical approaches that depend on geometry and thickness variations, electrochemical tuning enables fast, low-energy, and reversible modulation by regulating local carrier density, ion distribution, and interfacial gas content. From a transmission-line perspective, this strategy offers direct control over the complex impedance of the matching and absorbing layers without altering the device geometry, making it highly compatible with flexible and integrated systems. Furthermore, as shown in Fig. 4(f), the tunable device proposed in this study has great advantages in terms of effective bandwidth, modulation depth and cost (Table S1), which provided compelling evidence for the potential application of this device in wearable technology and integrated circuits.

2.4. Investigation of Mechanism for tunable device

The electrochemically driven multilayer intelligent wave absorber developed in this study demonstrates distinctive electrochemical behavior during its intricate charge-discharge cycle, particularly at the electrode interface of the air diffusion layer, where the in-situ dynamic generation and consumption of oxygen constitute a critical process [29,32]. In addition to this gas-mediated tuning, the Co-based catalyst embedded within the impedance-matching layer further enhances the electromagnetic response. As supported by recent studies on cobalt-containing absorbers, ultrafine CoO_x clusters dispersed in the N-doped mesoporous carbon matrix introduce complementary magnetic and dielectric loss channels, including interfacial polarization, dipole relaxation, and localized magnetic resonance, thereby promoting effective energy dissipation while maintaining favorable impedance matching [33-35]. In our device, these intrinsic loss mechanisms work synergistically with the electrochemically modulated oxygen environment. In this context, impedance matching refers to minimizing electromagnetic reflection at the air–material interface by adjusting the input impedance of the absorber (Z_{in}) to approach that of free space (Z_0). When $|Z_{in}/Z_0|$ approaches unity and the phase of Z_{in} is properly matched, reflection at the incident surface is suppressed, allowing more electromagnetic energy to penetrate into the multilayer structure, where it can be dissipated through dielectric and magnetic loss mechanisms. The impedance matching characteristics between the internal structure of the impedance matching layer and the external ambient air are not static but dynamically adjusted in response to variations in the device's operational state (Fig. 1). During the discharge phase of the tunable device, oxygen at the impedance matching layer serves as a pivotal raw material for the chemical reaction and is continuously consumed to sustain the internal electrochemical processes. As the oxygen concentration diminishes, the impedance matching between the impedance matching layer and the surrounding air deteriorates, as shown in Fig. 4(e). This mismatch weakens the interaction between incident electromagnetic waves and the device interface, resulting in increased reflection and reduced absorption. Such reflected waves not only degrade the absorbing performance but may also introduce electromagnetic interference into the surrounding environment.

Conversely, during the charging phase of the zinc-air battery, the air diffusion electrode becomes a site for oxygen generation. The continuous production and accumulation of oxygen markedly enhance the impedance matching between the electrode and the surrounding air. This optimized impedance matching facilitates smoother penetration of electromagnetic waves into the battery upon incidence on the electrode surface. Once inside, the waves undergo multiple diffuse reflections between the electrolyte layer and the zinc plate, extending their propagation path and enhancing their dissipation through the synergistic dielectric–magnetic loss mechanisms provided by both the device architecture and the CoO_x@NMC catalyst. As a result, electromagnetic leakage is effectively suppressed and the overall shielding performance is markedly improved. In summary, the dynamic changes in oxygen levels at the air diffusion electrode during the charge-discharge cycles of the

zinc-air battery induce significant variations in impedance matching, which profoundly influence the transmission and absorption behaviors of electromagnetic waves. These findings not only inform the electromagnetic compatibility design of battery systems but also offer novel insights into the development of efficient electromagnetic shielding materials and technologies.

Conclusion

This study proposes a multilayer tunable absorber based on electrochemical device and systematically investigates its operational mechanisms. The developed device demonstrates dynamically adjustable absorption characteristics across a broad frequency range spanning 6–18 GHz, achieving a peak modulation depth of 15 dB while maintaining consistent performance throughout rigorous six-hour operational stability tests. Furthermore, the structural integrity and stable electromagnetic response of the flexible tunable devices are preserved after 200 repeated bending cycles. The proposed design exhibits two distinctive advantages: continuous tunability through electrochemical modulation and wideband frequency adaptation, enabling effective electromagnetic shielding for precision electronic systems. From an application perspective, this solution offers a cost-effective platform with low energy consumption and facile processability, showing promising potential for next-generation wearable electronics, adaptive integrated circuits, intelligent home systems, and radar stealth technologies. The combination of mechanical flexibility, environmental stability, and tunable microwave absorption properties positions this device as a viable candidate for emerging electromagnetic compatibility applications in both civilian and military domains.

Experimental Section

Materials

Nitrogen-doped mesoporous carbon (NMC) was purchased from XFNANO Materials Tech Co. Ltd. Cobalt nitrate precursor ($Co(NO_3)_2{\cdot}6H_2O$, 99.9%), absolute ethanol (C_2H_5OH, 99.8%), Acrylamide (AM, 99.9%), N, N′-Methylene-bis(acrylamide) (MBAA, 99%) and Ammonium persulfate (APS, 98%) were purchased from Aladdin Company. Sodium alginate (SA, 99.9%) was purchased from Meryer Company.

Commercial 20 wt.% Pt/C, commercial RuO_2, Nafion perfluorinated resin solution (5 wt.%) and potassium hydroxide (KOH, 95%) were purchased from Sigma-Aldrich. All chemicals were of analytical reagent grade and used as received without further purification.

Preparation of CoO_x@NMC catalysts

The CoO_x@NMC catalysts were synthesized by a cascading process of grinding and thermal treatment. Typically, powders of 98.63 mg $Co(NO_3)_2{\cdot}6H_2O$ and 70 mg NMC were directly added into 20 mL of ethanol and sonicated in a high-power sonic bath to obtain a homogeneous suspension. The solution was then transferred to a mortar and ground into a uniform-colored mixture at room temperature. Subsequently, the mixture was thermally treated at 400°C for 2min with a rapid joule-heating process to obtain CoO_x@NMC catalyst under an air atmosphere.

Preparation of polymer electrolyte

The gel electrolyte was prepared via solution casting and free radical polymerization process. First, 4.21 g AM powder, 0.68 g SA powder, 15 mg APS powder and 8 mg MBAA were added to 30 mL deionized water under magnetic stirring at room temperature for 2h to form homogeneous solution. Then, the solution was poured into a square mold (100 × 100 × 10 mm^3) to make a thin PAM membrane. The as-prepared gel electrolyte was then immersed in mixed solution of 0.2 M $ZnCl_2$ + 6 M KOH.

Preparation of ZAB-based tunable device

A mixed solution of 0.2 M $ZnCl_2$ + 6 M KOH and a fresh polished Zn plate (500 μm thick) were used the electrolyte and anode, respectively. The air cathode consisted of a hydrophobic carbon paper with a gas diffusion layer (60 × 60 mm^2) on the air-facing side and a catalyst layer on the water-facing side. The catalyst layer was made by loading catalyst ink onto the carbon paper by drop-casting with a loading of 10 mg cm^{-2} for all catalysts. For the ZAB-based device, the anode and cathode were fixed between acrylic plates, and the electrolyte was injected into the intermediate compartment. The flexible device was assembled by sequentially stacking the cathode, hydrogel electrolyte, and metal anode, followed by vacuum sealing to ensure structural integrity and suppress electrolyte evaporation.

Material characterizations

Scanning electron microscope (SEM) was taken by a scanning transmission electron microscopy (FE-SEM, S-4800, Japan). Transmission electron microscopy (TEM) observations were performed on a transmission electron microscope (JEM-ARM200F, JEOL, Japan) operated at 200 kV. X-ray diffraction (XRD) patterns were recorded at room temperature using a D/max 2500V X-ray diffractometer (Rigaku, Japan) attached with Cu Kα radiation of a scanning speed of 8^o min^{-1}. XPS analysis was conducted using an X-ray photoelectron spectrometer (Escalab 250 Xi, Thermo Fisher Scientific, MA, USA) with an Al Kα radiation source (1487.6 eV) and a hemispherical analyzer operating at a pass energy of 30.0 eV and an energy step size of 0.05 eV. The C 1s peak at 284.8 eV served as the internal reference for binding energy calibration. Spectral deconvolution involved Shirley background subtraction and was performed using a Voigt function, combining Gaussian and Lorentzian components.

Electrochemical characterizations

All electro-catalytic tests were conducted in a conventional three-electrode electrochemical system containing 1 M KOH solution electrolyte at room temperature, using CHI 760 workstation in a standard three-electrode configuration. A rotating-disk glassy-carbon (area 0.196 cm^2) electrode coated with the catalyst ink served as the working electrode, while a graphite rod and saturated calomel electrode were employed as the counter electrode (CE) and reference electrode (RE), respectively. To prepare the working electrode, 5 mg powders of CoO_x@NMC was dispersed into the mixture solution of ethanol (100 μL) and DI water (800 μL) with 10 wt.% Nafion (100 μL) as the binder to form the catalyst ink and sonicated for 20 min. Then, 40 μL of the catalyst ink was drop-cast onto the surface of the GC electrode and dried in the air. For comparison, 5 mg of commercial 20% Pt/C and RuO_2 catalyst inks were also prepared in the same method. The potential, measured against a SCE electrode, was converted to the potential

versus the reversible hydrogen electrode (RHE) according to $E_{vs\ RHE} = E_{vs\ RE} + E^{\theta}_{RE} + 0.059\ pH$. Linear sweep voltammetry (LSV) curves were then recorded at a scan rate of 5 mV s^{-1} in 1 M KOH condition. For oxygen reduction reaction (ORR), RDE tests were performed in O_2-saturated 1 M KOH solution at 1600 rpm with a sweep rate of 10 mV s^{-1} at room temperature, after cyclic voltammetry (CV) activation for 30 cycles with a scan rate of 50 mV s^{-1} in N_2-saturated electrolyte.

Scattering parameters measurements

Scattering parameters (S-parameters) including S11, S22, S12, S21 are derived from direct measurement with a vector network analyzer (Keysight Technologies, N5524B). Permittivity and permeability were also measured by the same vector network analyzer. The A (absorption coefficient), R (reflection coefficient), T (transmission coefficient) were calculated from the S-parameters according to the following equations:

$R+A+T=1$ (1)

$R=|S_{11}|^2$ (2)

$T=|S_{21}|^2$ (3)

$SE_T = -10\log_{10}(|S_{21}|^2)$ (4)

$Z_{in} = Z_0 \cdot \frac{1-S_{11}}{1+S_{11}}$ (5)

$Z_{out} = Z_0 \cdot \frac{1-S_{22}}{1+S_{22}}$ (6)

Z_{in}: input impedance of the sample.

Z_0: free-space impedance.

Electronic Supplementary Material: Supplementary material (please provide the brief detail of the ESM) is available in the online version of this article at https://doi.org/10.26599/NR.2026.94908383.

Data availability

All data needed to support the conclusions in the paper are presented in the manuscript and/or the Electronic Supplementary Material. Additional data related to this paper may be requested from the corresponding author upon request.

Acknowledgements

This work was supported by the National Natural Science Foundation of China (Grant No. 52472087, 52325312, 52388201, 92472106 and 52421001), the Fundamental Research Funds for the Central Universities (Grant No. 2023ZCJH03 and 2021XD-A041), Beijing Natural Science Foundation (Grant No. JQ22010 and L253008), National Natural Science Foundation of China (Grant No. U2241243), Fund of State Key Laboratory of Information Photonics and Optical Communications (Beijing University of Posts and Telecommunications, P.R. China), State Key Laboratory of New Ceramic Materials Tsinghua University (Grant No. 2025QHTC-ZZKYA003 and KF202528), R&D Program of Zhejiang (Grant No. 2024C01195) and State Key Laboratory of IPOC (BUPT) (Grant No. IPOC2024ZT13).

Declaration of competing interest

All the contributing author(s) report(s) no conflict of interests in this work.

Author contribution statement

Xinyu Xie: Data curation, investigation, project administration, validation, writing-origin draft, experimental design, formal analysis, visualization. Yufeng Wu: Investigation, supervision, validation, review. Yunzhi Li: Investigation, data curation. Anqi Li: Data curation, formal analysis. Jiaoyang Gong: Data curation, formal analysis. Chang Li: Formal analysis. Zhuting Zhang, Hsiang-shun Chang, Yan Feng, Tianyi Wang: Formal analysis. Jianchun Xu, Peng Du, Hehe Wei, Ming Lei, Ke Bi: Supervision, validation. Yunjian Guo: Supervision, writing - review & editing. Kai Huang, Hui Wu: Conceptualization, funding acquisition, project administration, resources, writing - review & editing. All the authors have approved the final manuscript.

Use of AI statement

During the preparation of this work, the authors used ChatGPT in order to polish the language and check the grammar. After using this tool/service, the authors reviewed and edited the content as needed and take full responsibility for the content of the publication.

References

[1] Hou, T.; Wang, B.; Jia, Z.; Wu, H.; Lan, D.; Huang, Z.; Feng, A.; Ma, M.; Wu, G. A review of metal oxide-related microwave absorbing materials from the dimension and morphology perspective. J. Mater. Sci.: Mater. Electron. **2019**, 30, 10961-10984.

[2] Yang, Y.; Wu, N.; Li, B.; Liu, W.; Pan, F.; Zeng, Z.; Liu, J. Biomimetic Porous MXene Sediment-Based Hydrogel for High-Performance and Multifunctional Electromagnetic Interference Shielding. ACS Nano. **2022**, 16, 15042-15052.

[3] Jia, Z.; Lin, K.; Wu, G.; Xing, H.; Wu, H. Recent Progresses of High-Temperature Microwave-Absorbing Materials. Nano. **2018**, 13, 1830005.

[4] Dai, C.; Li, X.; Yang, W. X.; Chen, Y.; Zheng, D.; Cheng, N.; Shui, T.; Zhang, H.; Li, Z. Dynamic Wavelength - Selective Diffraction and Absorption with Direct-Patterned Hydrogel Metagrating. Adv. Sci. **2024**, 11, 2408960.

[5] Lv, H. L.; Yang, Z. H.; Pan, H. G.; Wu, R. B. Electromagnetic absorption materials: Current progress and new frontiers. Prog. Mater. Sci. **2022**, 127, 52–64.

[6] Liu, X.; Liu, H.; Wu, H.; Zhou, Q.; Liang, H.; Liu, G.; Duan, W.; Gu, Y.; Xu, C.; Travitzky, N.; Colombo, P.; Riedel, R. Structural Electromagnetic Absorber Based on MoS_2/PyC - Al_2O_3 Ceramic Metamaterials. Small. **2023**, 19, 2300664.

[7] Qin, M.; Zhang, L.; Wu, H. Dielectric Loss Mechanism in Electromagnetic Wave Absorbing Materials. Adv. Sci. **2022**, 9, 2105553.

[8] Hu, N.; Zhang, J.; Zha, S.; Liu, C.; Liu, H.; Liu, P. Design of a Multilayer Broadband Switchable Absorber Based on Semiconductor Switch. IEEE Antennas Wireless Propag. Lett. **2019**, 18, 373-377.

[9] Chen, P.; He, S.B.; Wang, T. Y.; Wang, C. C.; Tao, J. R.; Li, Y. W. Melanin-like nanofibers with highly ordered structures achieve ultrahigh specific electromagnetic interference shielding efficiency. Nat. Commun. **2025**, 16, 7127.

[10] Chen, P.; He, S.; Zou, Z.; Wang, T.; Hu, J.; Tao, J.; Yang, L.; Li, Y.

Intelligent Hydrogels Enabled Large-Scale Variability in Continuously Tunable Microwave Absorption. Adv. Funct. Mater. **2025**, 2506308.

[11] Wang, J. N.; Xiong, B.; Peng, R. W.; Li, C. Y.; Hou, B. Q.; Chen, C. W.; Liu, Y.; Wang, M. Flexible Phase Change Materials for Electrically-Tuned Active Absorbers. Small. **2021**, 17, 2101282.

[12] Wang, Z. Y.; Li, Z. C.; Li, B.; Shi, A. F.; Zhang, L.; Zhu, Y. B.; Ye, F.; Yu, S. H. Functional Carbon Springs Enabled Dynamic Tunable Microwave Absorption and Thermal Insulation. Adv. Mater. **2024**, 36, 2412605.

[13] Li, A.; Kim, S.; Luo, Y.; Li, Y.; Long, J.; Sievenpiper, D. F. High-Power Transistor-Based Tunable and Switchable Metasurface Absorber. IEEE TMTT. **2017**, 65, 2810-2818.

[14] Fang, M.; Huang, L.; Cui, Z.; Yi, P.; Zou, H.; Li, X.; Deng, G.; Chen, C.; Geng, Z.; He, J.; Sun, X.; Shui, J.; Yu, R.; Liu, X. Phase-Transition Microcapacitor Network in Organohydrogel for Absorption-Dominated Electromagnetic Interference Shielding and Multi-Mode Intelligent Responsiveness. Adv. Funct. Mater. **2025**, 35, 2418870.

[15] Zhao, Z.; Zhang, L.; Wu, H. Hydro/Organo/Ionogels: "Controllable" Electromagnetic Wave Absorbers. Adv. Mater. **2022**, 34, 2205376.

[16] Strand, M. T.; Hernandez, T. S.; Danner, M. G.; Yeang, A. L.; Jarvey, N.; Barile, C. J. McGehee, M. D.; Polymer inhibitors enable >900 cm^2 dynamic windows based on reversible metal electrodeposition with high solar modulation. Nat. Energy. **2021**, 6, 546-554.

[17] Han, M.; Zhang, D.; Shuck, C. E.; McBride, B.; Zhang, T.; Wang, R.; Shevchuk, K.; Gogotsi, Y. Electrochemically modulated interaction of MXenes with microwaves. Nat. Nanotechnol. **2023**, 18, 373-379.

[18] Guo, Y.; Bae, J.; Fang, Z.; Li, P.; Zhao, F.; Yu, G. Hydrogels and Hydrogel-Derived Materials for Energy and Water Sustainability. Chem. Rev. **2020**, 120, 7642-7707.

[19] Huang, K.; Wang, R.; Zhao, S.; Du, P.; Wang, H.; Wei, H.; Long, Y.; Deng, B.; Lei, M.; Ge, B.; Gou, H.; Zhang, R.; Wu, H. Atomic species derived CoO_x clusters on nitrogen doped mesoporous carbon as advanced bifunctional electro-catalysts for Zn-air battery. Energy Storage Materials. **2020**, 29, 156-162.

[20] Xu, W.; Lyu, F.; Bai, Y.; Gao, A.; Feng, J.; Cai, Z.; Yin, Y. Porous cobalt oxide nanoplates enriched with oxygen vacancies for oxygen evolution reaction. Nano Energ. **2018**, 43, 110-116.

[21] Shi, Z.; Chen, S.; Xu, Z.; Liu, Z.; Guo, J.; Yin, J.; Xu, P.; Zhang, N.; Zhang, W.; Alshareef; H. N.; Liu; T. Metal Oxide Aerogels: A New Horizon for Stabilizing Anodes in Rechargeable Zinc Metal Batteries. Adv. Energy Mater. **2023**, 13, 2300331.

[22] Liu, J.-N.; Zhao, C.-X.; Wang, J.; Fang, X. Q.; Bi, C.-X.; Li, B. Q.; Zhang, Q. A data-driven bifunctional oxygen electrocatalyst with a record-breaking ΔE = 0.57 V for ampere-hour-scale zinc-air batteries. Joule. **2024**, 8, 1804-1819.

[23] Leong, K. W.; Wang, Y.; Ni, M.; Pan, W.; Luo, S.; Leung, D. Y. C. Rechargeable Zn-air batteries: Recent trends and future perspectives. Renew. Sustain. Energy Rev. **2022**, 154, 111771.

[24] Bao, B.; Zeng, Q.; Li, K.; Wen, J.; Zhang, Y.; Zheng, Y.; Zhou, R.; Shi, C.; Chen, T.; Xiao, C.; Chen, B.; Wang, T.; Yu, K.; Sun, Y.; Lin, Q.; He, Y.; Tu, S.; Zhu, L. Rapid fabrication of physically robust hydrogels. Nat. Mater. **2023**, 22, 1253-1260.

[25] Lv, Y.; Zhao, M.; Du, Y.; Kang, Y.; Xiao, Y.; Chen, S. Engineering a self-adaptive electric double layer on both electrodes for high-performance zinc metal batteries. Energy Environ. Sci. **2022**, 15, 4748-4760.

[26] Zhao, S.; Zuo, Y.; Liu, T.; Zhai, S.; Dai, Y.; Guo, Z.; Wang, Y.; He, Q.; Xia, L.; Zhi, C.; Bae, J.; Wang, K.; Ni, M. Multi-Functional Hydrogels for Flexible Zinc-Based Batteries Working under Extreme Conditions. Adv. Energy Mater. **2021**, 11, 2101749.

[27] Li, W.; Cheng, L.; Chen, X.; Liu, Y.; Liu, Y.; Liu, Q.; Huang, Y. Key materials and structural design in flexible and stretchable zinc-air batteries. Nano Energy. **2023**, 106, 108039.

[28] Zhu, T.; Jiang, C.; Wang, M.; Zhu, C.; Zhao, N.; Xu, J. Skin-Inspired Double-Hydrophobic-Coating Encapsulated Hydrogels with Enhanced Water Retention Capacity. Adv. Funct. Mater. **2021**, 31, 2102433.

[29] Li, X.; Wang, X.; Li, M.; Zhu, W.; Luo, H.; Lu, X.; Xu, H.; Xue, J.; Ye, F.; Wu, H.; Fan, X. Built-In Electric Field Enhancement Strategy Induced by Cross-Dimensional Nano-Heterointerface Design for Electromagnetic Wave Absorption. Adv. Funct. Mater. **2025**, 35, 2407217.

[30] Zhang, S.; Zheng, J.; Lan, D.; Gao, Z.; Liang, X.; Tian, Q.; Zhao, Z.; Wu, G. Hierarchical Engineering on Built-In Electric Field of Bimetallic Zeolitic Imidazolate Derivatives Towards Amplified Dielectric Loss. Adv. Funct. Mater. **2025**, 35, 2413884.

[31] Zhou, G.; Wang, P.; Li, H.; Hu, B.; Sun, Y.; Huang, R.; Liu, L. Spin-state reconfiguration induced by alternating magnetic field for efficient oxygen evolution reaction. Nat. Commun. **2021**; 12, 4827.

[32] Yan, J.; Wang, Y.; Zhang, Y.; Xia, S.; Yu, J.; Ding, B. Direct Magnetic Reinforcement of Electrocatalytic ORR/OER with Electromagnetic Induction of Magnetic Catalysts. Adv. Mater. **2021**, 33, 2007525.

[33] Yao, L. H.; Shu, J. C.; Zhao, J. G.; Zong, J. Y.; Cao, M. S.; Cao, W. Q. Heterodimensional Structure Integrating Electromagnetic Functions and Hybrid Energy Storage to Drive Multifunctional Devices. Adv. Funct. Mater. **2025**, 35, 2503307.

[34] Yao L.; Wang Y.; Zhao J.; Zhu Y.; Cao M. Multifunctional Nanocrystalline-Assembled Porous Hierarchical Material and Device for Integrating Microwave Absorption, Electromagnetic Interference Shielding, and Energy Storage. Small. **2023**, 19, 2208101.

[35] Xu J.; Xu X. Y.; Ma Z.; Zhang X.; Yan F.; Yang P. P.; Zhu C.L.; Chen, Y.J. Heterointerface engineering of N-doped graphene aerogels anchored with ultra-small Co and MnO nanoparticles for excellent electromagnetic wave absorption. Carbon, **2024**, 228, 119409.

[36] Zhao, P. Y.; Peng, H. L.; Cai, B.; Zhou, L.; Liang, C. M.; Koo, M. C.; Wang, H. Y.; Wu, J.; Hou, Z. L.; Wang, G. S. Mechanism decoupling of impedance matching and attenuation enhancement via spatial distribution of loading components. Adv. Func. Mat. **2025**, e18479.

[37] Liang, C.; Hou, Z.; Koo, M. C.; Xu, F.; Bai, S.; Bai, Y.; Zhang, Y.; Cai, B.; Zhao, P.; Wang, G. Modulating electromagnetic response through the regulation of built-in electric fields. J. M. S. T. **2025**, 244, 126–134.

[38] Zhou, L.; Hu, P.; Bai, M.; Leng, N.; Cai, B.; Peng, H. L.; Zhao, P. Y.; Guo, Y.; He, M.; Wang, G. S.; Gu, J. Harnessing the electronic spin states of single atoms for precise electromagnetic modulation. Adv. Mat. **2025**, 37, 2418321.

[39] Wu, Y.; Li, Q.; Li, Y.; Li, C.; Zhou, Y.; Du, P.; Cao, W.; He, X.; Liu, Z.; Xu, J.; Huang, K.; Lei, M.; Bi, K.; Wu, H. Roll-to-roll joule-heating to construct ferromagnetic carbon fiber felt for superior electromagnetic interference shielding. Carbon. **2024**; 229, 119474.

[40] Reinhold, L. RF circuit design: theory and applications; Upper Saddle River. NJ : Prentice-Hall. **2000**.

Electronic Supplementary Material

Tunable microwave absorption driven by electrochemically air-breathing

Xinyu Xie[1,2], Yufeng Wu[1,2,3], Yunzhi Li[1,2], Anqi Li[1,2], Jiaoyang Gong[1,2], Chang Li[1,2], Zhuting Zhang[2], Hsiang-shun Chang[2], Yan Feng[2], Tanyi Wang[1,2], Peng Du[4], Hehe Wei[2], Jianchun Xu[1], Yunjian Guo[1], Kai Huang[1]✉, Ming Lei[1,5], Ke Bi[1]✉, and Hui Wu[2,3]✉

[1] *State Key Laboratory of Information Photonics and Optical Communications, School of Physical Science and Technology, Beijing University of Posts and Telecommunications, Beijing100876, China*
[2] *State Key Laboratory of New Ceramic Materials, School of Materials Science and Engineering, Tsinghua University, Beijing 100084, PR China*
[3] *Wuzhen Laboratory, Tongxiang 314500, China*
[4] *Zhejiang Key Laboratory for Island Green Energy and New Materials, Institute of Electrochemistry, School of Materials Science and Engineering, Taizhou University, Taizhou 318000, China*
[5] *State Key Laboratory of Information Photonics and Optical Communications & School of Integrated Circuits, Beijing University of Posts and Telecommunications, Beijing 100876, China*

✉Address correspondence to Kai Huang, huang-kai@bupt.edu.cn; Ke Bi, bike@bupt.edu.cn; Hui Wu, huiwu@tsinghua.edu.cn

Supporting information to https://doi.org/10.26599/NR.2026.94908383

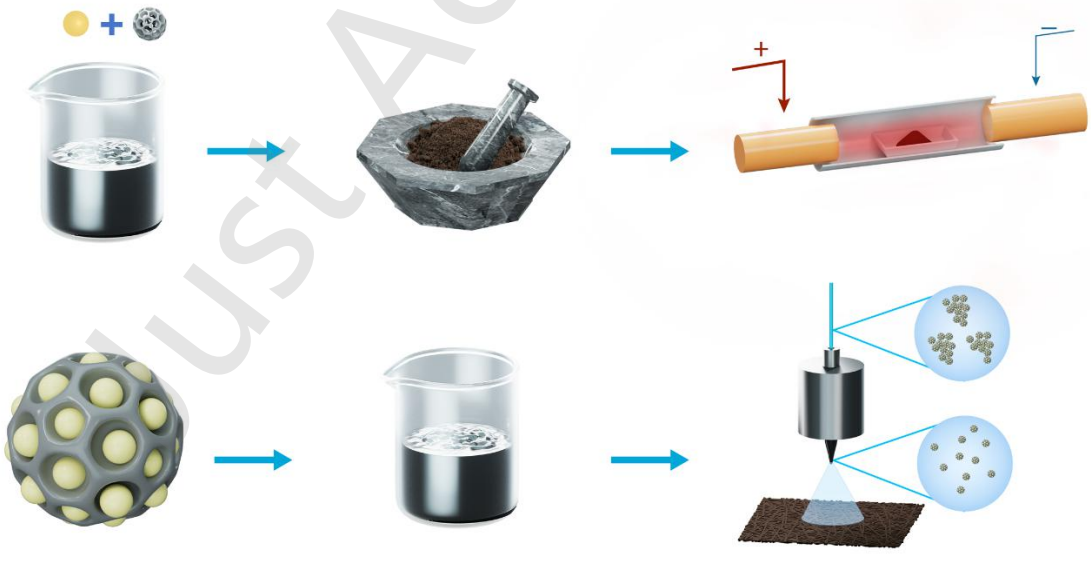

Figure S1. Schematic illustration of the synthesis process of the catalyst CoO_x@NMC.

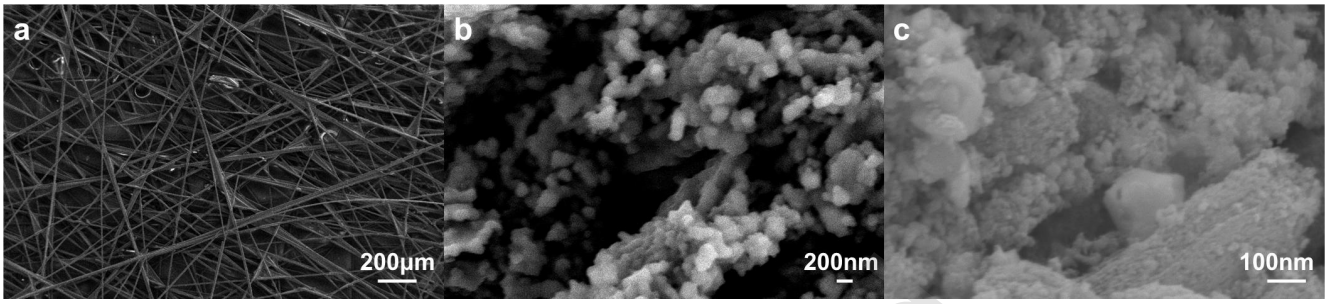

Figure S2. (a) The SEM images of the air diffusion layer. (b-c) The SEM images of synthesized CoO_x@NMC at different magnifications.

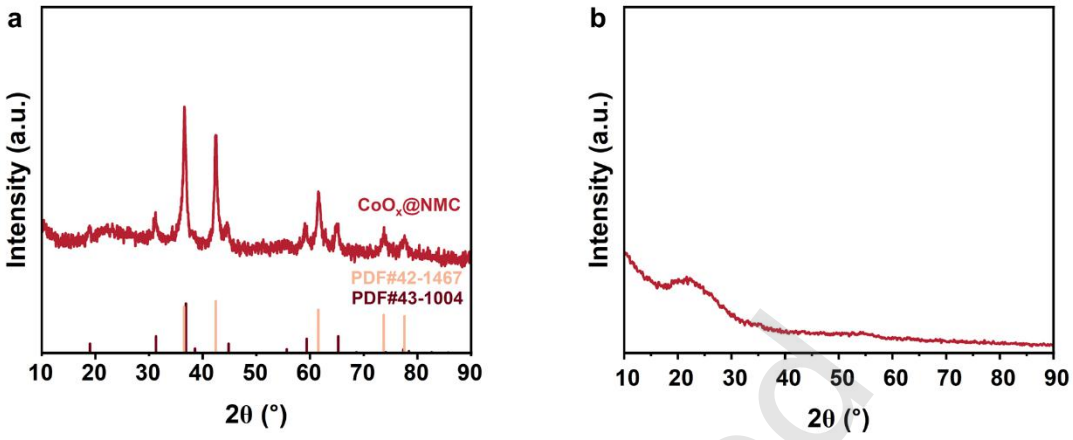

Figure S3. (a) The XRD patterns of CoO_x@NMC. b) XRD patterns of NMC.

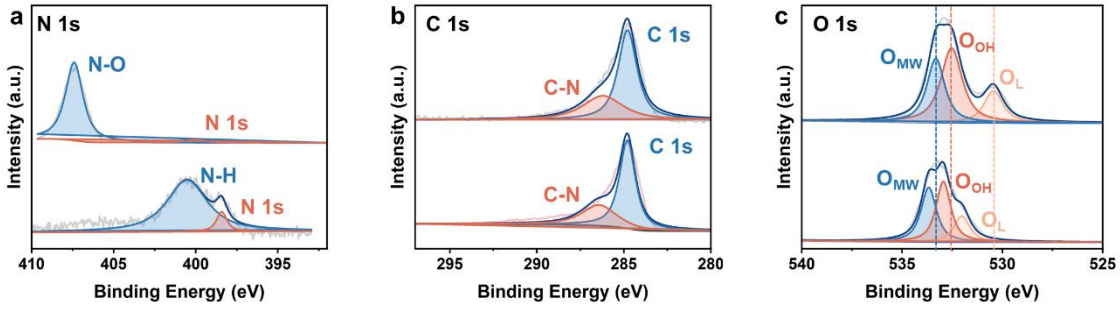

Figure S4. (a-b) The high-resolution N 1s, C 1s XPS spectra of CoO_x@NMC and pristine NMC. (c) The high-resolution O 1s XPS spectra of CoO_x@NMC and pristine Co $(NO_3)_2$.

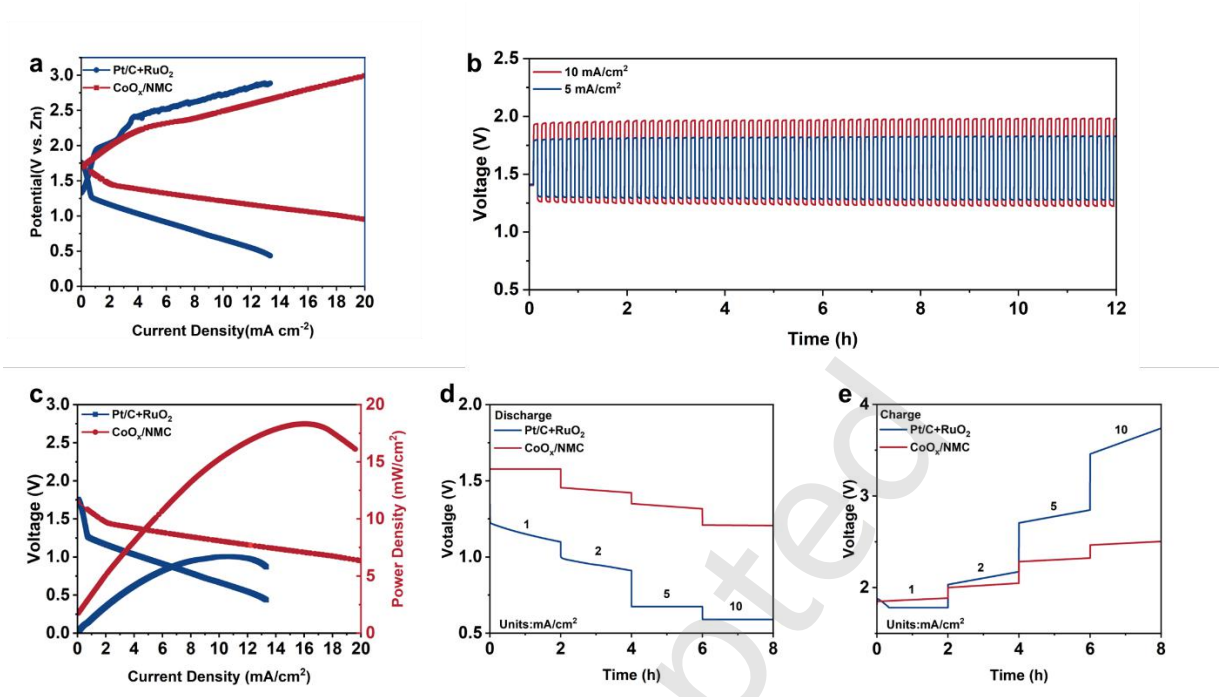

Figure S5. (a) Charge and discharge polarization curves of synthesized and commercial catalysts. (b) ZAB-based device cycling test at different charging and discharging current densities. (c) Power density and polarization plots of synthesized and commercial catalysts. (d-e) Step charging and discharging curve of synthesized and commercial catalysts.

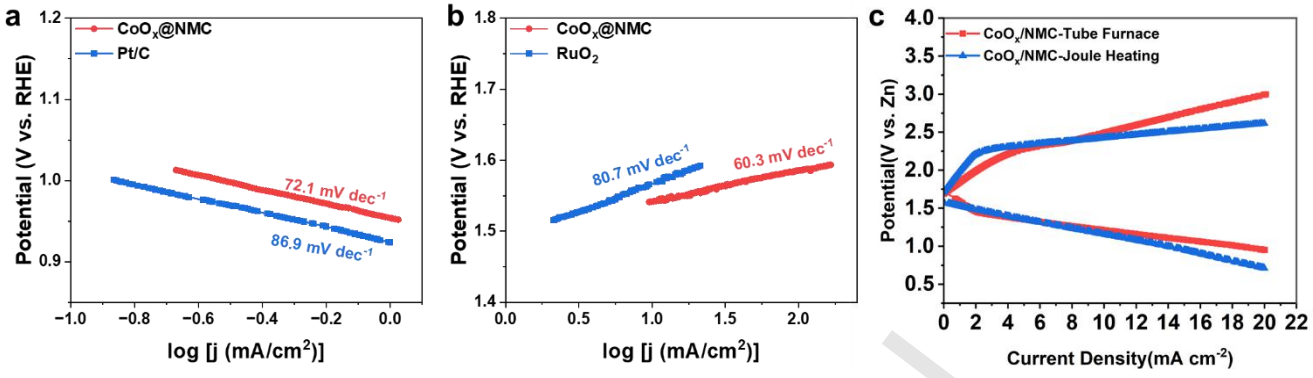

Figure S6. Tafel plots of (a) the corresponding ORR polarizations curves and (b) the corresponding OER polarizations curves. (c) Charge and discharge polarization curves of catalyst synthesized at different condition.

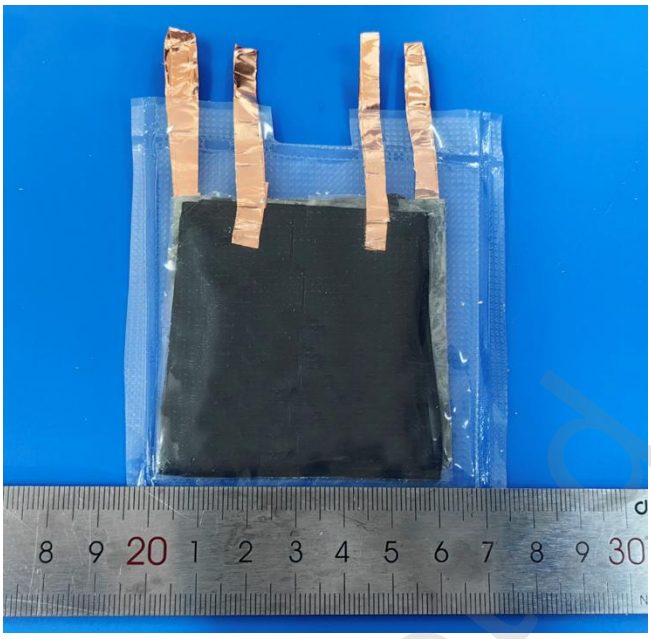

Figure S7. The image of as-prepared flexible device.

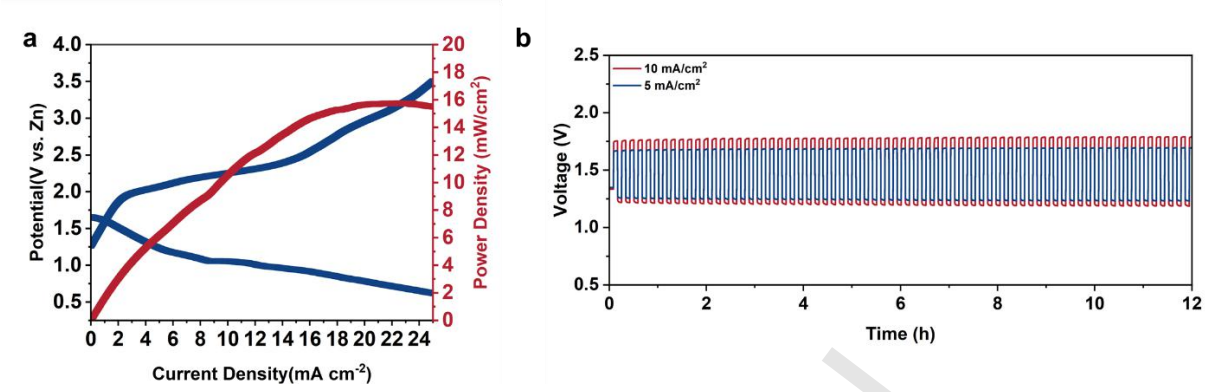

Figure S8. (a) Charge and discharge polarization curves of synthesized catalysts in flexible device. (b) Flexible device cycling test at different charging and discharging current densities.

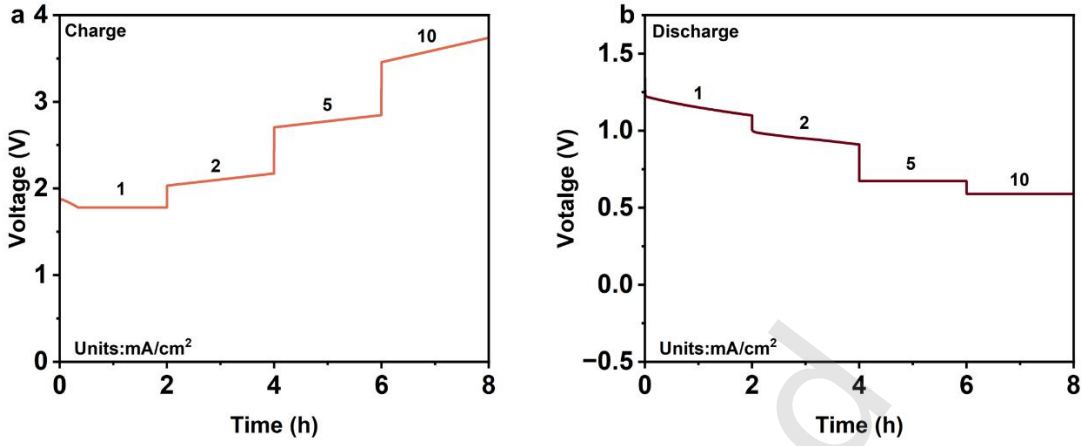

Figure S9. (a-b) Step charging and discharging curve of synthesized catalysts in flexible device.

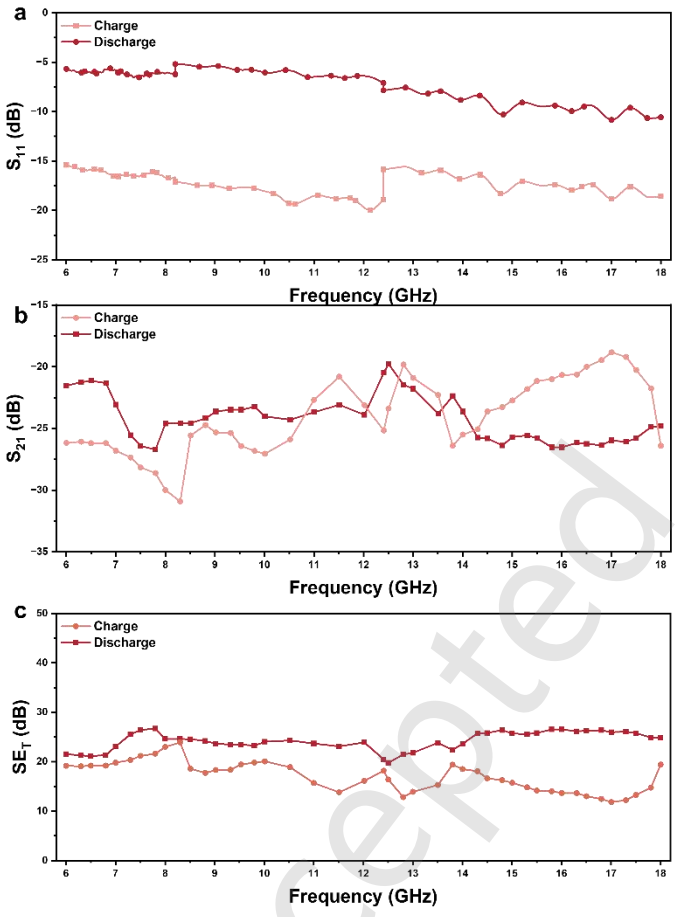

Figure S10. (a-b) S parameter of the flexible device. (c) SET curve of the flexible device.

Table S1. Comparison of the properties of different mechanisms.

Modulation type	Material	Modulation depth	Effective absorption band width	Flexibility	Ref
Meta surface	VGCFs/PDMS-EP	-23.5dB~-55.7dB	9.8GHz	4	[1]
	ITO/water-based meta surface	≥-10dB	85.72 GHz	1	[2]
	SMPs-based absorber	-1.34dB~-17dB	2.2GHz	1	[3]
Electrochemical deposition	polyamide@carbon/Fe_3O_4 fibers	-5dB~-50.31 dB	5.2 GHz	4	[4]
	Ag/Pt	-1.2dB~-13dB	6GHz	1	[5]
Temperature modulation	CNTs/VO_2/ANF	-8dB~-12dB	3.70GHz	3	[6]
	3D Ni chain	-15.28dB~-50 dB（373 K）	4.2GHz	1	[7]
	$BiFeO_3$	-20dB~-39 dB	/	1	[8]
Deformation regulation	CNCs/CF	-17dB~-64.6 dB	15.4 GHz	4	[9]
	Functional carbon spring	-24dB~-35 dB	13.4 GHz	3	[10]
	PI@CNCs/CF	-13dB~-60.5 dB	10.8 GHz	3	[11]
	Elastic carbon aerogel derived from chitin nanofibers	-37dB~-40 dB	4.2 GHz	3	[12]
	CF@TiO_2/C Aerogels	-15.08dB~-74.38dB	7.84 GHz	3	[13]
	Biomimetic ionic gel	-2.1dB~-43.6 dB	X band	4	[14]
	CNT film	-13.60dB~-47.66 dB	4.4GHz	4	[15]
	PDMAPS/AC	≈97.5%	200-2500nm	4	[16]
	PVA/PMMA/AC	＞95%	0-2000nm	4	[17]
Electrochemically modulation	**CoO_x@NMC**	**15 dB**	**12 GHz**	**4**	**This work**

The following were the rating metrics we defined:
Flexibility: foldable + bendable=4, bendable and rebound=3, bendable but not rebound=2, no flexibility=1.

Table S2. Comparison of the catalytic properties of different materials.

Material	Electrolyte	Overpotential (mV) at 10 mA cm^{-2}	Tafel Slope (mV dec^{-1})	Bifunctionality	Refs.
Co_3O_4@C/GPO	1.0 M H_2SO_4	360	143	√	[18]
FTO@Co_3O_4/CP	0.5 M H_2SO_4	511	104	×	[19]
Co_3O_4@FTO/CP	0.5 M H_2SO_4	646	/	×	[20]
Co@Co_3O_4@N–CNTs	1.0 M KOH	296	116.2	×	[21]
Co_3O_4– Mo_2N	1.0 M KOH	300	164	×	[22]
Co_3O_4/rGO	1.0 M KOH	346	47	×	[23]
NP-Co3O4/CC	1.0 M KOH	330	/	√	[24]
Co_3O_4/NPC	1.0 M KOH	390	58	√	[25]
CMO@CNTs	1.0 M KOH	270	81.1	√	[26]
CMO/NCNF	1.0 M KOH	340	93.5	√	[27]
Co_3O_{4-x}/GO	0.1 M KOH	280	/	√	[28]
Mn_x-Co_3O_4/C	0.5 M H_2SO_4	431	73.7	×	[29]
Cu_2S–CoO_x/CF	10 M KOH	255	136	×	[30]
This work	1.0 M KOH	357	60.3	√	

Table S3. Comparison of the wave absorption properties of different materials.

Cobalt-based absorber material	d（mm）	RL（dB）	EAB（GHz）	Ref
Co_3O_4/carbon	2.0	-36.27	/	[31],[32]
Co_3O_4 / GNs	3.4	-52.46	3.52	[33]
NF@Co_3O_4	2.3	-41.1	3.46	[34],[35]
$C(OH)_2$_Co_3O_4/graphene	1.92	-56.9	5.9	[36],[37]
$C(OH)_2$_Co_3O_4/MWCNT	2.03	-55.8	2.16	[36],[38]
$C(OH)_2$_Co_3O_4/Carbon black	4.60	-37.1	1.36	[36],[38]
Co_3O_4/MWCNT/graphene ternary	1.74	-19.6	1.28	[36],[38]
2D Co_3O_4 porous graphitic carbon nanosheet	1.5	-50.0	4.2	[36],[39]
CoO_x/CFs	1.5	-45.16	/	[40]
CNFs@carbonaceous Co/CoO	3.54	-53.1	/	[41]
CoO/Co@C	1.5	-38.46	4.8	[42]

References

[1] Li, X.; Zhu, Y.; Liu, X.; Bin Xu, B.; Ni, Q. A broadband and tunable microwave absorption technology enabled by VGCFs/PDMS-EP shape memory composites. Composite Structures. **2020**, 238.

[2] Ge, J.; Zhang, Y.; Li, H.; Dong, H.; Zhang, L. Ultra - Broadband, Tunable, and Transparent Microwave Meta - Absorber Using ITO and Water Substrate. Advanced Optical Materials. **2023**, 11.

[3] Yi, J.; Wei, M.; Lin, M.; Zhao, X.; Zhu, L.; Chen, X.; Jiang, Z. H. Frequency-Tunable and Magnitude-Tunable Microwave Metasurface Absorbers Enabled by Shape Memory Polymers. IEEE Transactions on Antennas and Propagation. **2022**, 70, 6804-6812.

[4] Deng, X.; Gao, S.; Qi, X.; Dai, H.; Fu, S.; Ni, Q.; Fu, Y. Scalable 3D textile with hierarchically functionalized pyramidal units using nanostructured polyamide@carbon/Fe_3O_4 fibers for tunable microwave absorption. Chemical Engineering Journal. **2023**, 473.

[5] Meng, Z.; Liu, D.; Xing, S.; Pang, Y.; Jia, Y.; Li, M.; Zu, M.; Wang, Z.; Liu, T.; Cheng, H. Tunable Microwave Absorbing Devices Enabled by Reversible Metal Electrodeposition. ACS Applied Materials & Interfaces. **2024**, 16, 11686-11693.

[6] Wang, S.; Hao, X.; Liu, Y.; Cheng, Z.; Chen, S.; Peng, G.; Tao, J.; Yao, J.; Yang, F.; Zhou, J.; Intelligent Tunable Wave-Absorbing CNTs/VO_2/ANF Composite Aerogels Based on Temperature-Driving. ACS Applied Materials & Interfaces. **2024**, 16, 32773-32783.

[7] Liu, J.; Cao, M.-S.; Luo, Q.; Shi, H.-L.; Wang, W.-Z.; Yuan, J. Electromagnetic Property and Tunable Microwave Absorption of 3D Nets from Nickel Chains at Elevated Temperature. ACS Applied Materials & Interfaces. **2016**, 8, 22615-22622. https://doi.org/10.1021/acsami.6b05480.

[8] Li, Y.; Fang, X.; Cao, M. Thermal frequency shift and tunable microwave absorption in $BiFeO_3$ family. Scientific Reports. **2016**, 6.

[9] Wu, L.; Shi, S.; Wang, G.; Mou, P.; Liu, X.; Liu, J.; Li, L.; Du, C. Carbon Nanocoils/Carbon Foam as the Dynamically Frequency - Tunable Microwave Absorbers with an Ultrawide Tuning Range and Absorption Bandwidth. Advanced Functional Materials. **2022**, 32.

[10] Wang, Z. Y.; Li, Z. C.; Li, B.; Shi, A. F.; Zhang, L.; Zhu, Y. B.; Ye, F.; Yu, S. H. Functional Carbon Springs Enabled Dynamic Tunable Microwave Absorption and Thermal Insulation. Advanced Materials. **2024**, 36.

[11] Liu, X.; Wu, L.; Liu, J.; Lv, H.; Mou, P.; Shi, S.; Yu, L.; Wan, G.; Wang, G. Dynamically frequency - tunable and environmentally stable microwave absorbers. Carbon Energy. **2024**, 6.

[12] Li, X.; Zhu, L.; Kasuga, T.; Nogi, M.; Koga, H. Frequency-tunable and absorption/transmission-switchable microwave absorber based on a chitin-nanofiber-derived elastic carbon aerogel. Chemical Engineering Journal. **2023**, 469.

[13] Wu, F.; Hu, F.; Hu, P.; Zhang, P.; Fan, B.; Kong, H.; Zheng, W.; Cai, L.; Sun, Z. Multifunctional carbon Fiber@TiO_2/C aerogels derived from MXene for pressure tunable microwave absorption. Carbon. **2024**, 230.

[14] Yang, H.; Tan, Y.; Zhang, Y.; Xiong, Y.; Nie, G.; Luo, H.; He, P.; Yang, J.; Zhao, X.; Tong, J.; Zhang, Y. Bionic Scarfskin-Inspired Hierarchy Configuration toward Tunable Microwave-Absorbing Performance. ACS Applied Materials & Interfaces. **2022**, 14, 16669-16677.

[15] Sun, H.; Che, R.; You, X.; Jiang, Y.; Yang, Z.; Deng, J.; Qiu, L.; Peng, H. Cross - Stacking Aligned Carbon - Nanotube Films to Tune Microwave Absorption Frequencies and Increase Absorption Intensities. Advanced Materials. **2014**, 26, 8120-8125.

[16] Lei, C.; Guan, W.; Guo, Y.; Shi, W.; Wang, Y.; Johnston, K. P.; Yu, G. Polyzwitterionic Hydrogels for Highly Efficient High Salinity Solar Desalination. Angewandte Chemie International Edition. **2022**, 61, e202208487.

[17] Guo, Y.; de Vasconcelos, L. S.; Manohar, N.; Geng, J.; Johnston, K. P.; Yu, G. Highly Elastic Interconnected Porous Hydrogels through Self-Assembled Templating for Solar Water Purification. Angewandte Chemie International Edition. **2022**, 61, e202114074.

[18] Yu, J.; Garcés-Pineda, F. A.; González-Cobos, J.; Peña-Díaz, M.; Rogero, C.; Giménez, S.; Spadaro, M. C.; Arbiol, J.; Barja, S.; Galán-Mascarós, J. R. Sustainable Oxygen Evolution Electrocatalysis in Aqueous 1 M H2SO4 with Earth Abundant Nanostructured Co_3O_4. Nat. Commun. **2022**, 13.

[19] Yeh, Y. X.; Cheng, C. C.; Jhu, P. S.; Lin, S. H.; Chen, P. W.; Lu, S. Y. Core–Shell FTO@Co_3O_4 Nanoparticles as Active and Stable Anode Catalysts for Acidic Oxygen Evolution Reaction and Proton Exchange Membrane Water Electrolysis. Journal of Materials Chemistry A. **2023**, 11 3399–3407.

[20] Wang, Q.; Zhao, S.; Yu, H.; Zhang, D.; Wang, Q. Synergistic Engineering of Defects and Architecture in a Co@Co_3O_4@N-CNT Nanocage toward Li-Ion Batteries and HER. Inorganic Chemistry. **2022**, 61, 19567–19576.

[21] Wang, T.; Wang, P.; Zang, W.; Li, X.; Chen, D.; Kou, Z.; Mu, S.; Wang, J. Nanoframes of Co_3O_4–Mo_2N Heterointerfaces Enable High-Performance Bifunctionality toward Both Electrocatalytic HER and OER. Advanced Functional Materials. **2021**, 32.

[22] Leng, M.; Huang, X.; Xiao, W.; Ding, J.; Liu, B.; Du, Y.; Xue, J. Enhanced Oxygen Evolution Reaction by Co-O-C Bonds in Rationally Designed Co_3O_4/Graphene Nanocomposites. Nano Energy. **2017**, 33, 445–452.

[23] Wang, X.; Liao, Z.; Fu, Y.; Neumann, C.; Turchanin, A.; Nam, G.; Zschech, E.; Cho, J.; Zhang, J.; Feng, X. Confined Growth of Porous Nitrogen-Doped Cobalt Oxide Nanoarrays as Bifunctional Oxygen Electrocatalysts for Rechargeable Zinc–Air Batteries. Energy Storage Materials. **2020**, 26, 157–164.

[24] Sun, J.; Yang, Y.; Wang, J.; Zhang, Z.; Guo, J. In-Situ Construction of Cobalt Oxide/ Nitrogen-Doped Porous Carbon Compounds as Efficient Bifunctional Catalysts for Oxygen Electrode Reactions. Journal of Alloys and Compounds. **2020**, 827, 154308.

[25] Ma, T.; Li, C.; Chen, X.; Cheng, F.; Chen, J. Spinel Cobalt–Manganese Oxide Supported on Non-Oxidized Carbon Nanotubes as a Highly Efficient Oxygen Reduction/Evolution Electrocatalyst. Inorganic Chemistry Frontiers. **2017**, 4, 1628–1633.

[26] Chen, X.; Yan, Z.; Yu, M.; Sun, H.; Liu, F.; Zhang, Q.; Cheng, F.; Chen, J. Spinel Oxide Nanoparticles Embedded in Nitrogen-Doped Carbon Nanofibers as a Robust and Self-Standing Bifunctional Oxygen Cathode for Zn–Air Batteries. Journal of Materials Chemistry A. **2019**, 7, 24868–24876.

[27] Sun, Y.; Wang, Q.; Liu, Z. Bifunctional OER/NRR Catalysts Based on a Thin-Layered Co_3O_4–x/GO Sandwich Structure. ACS

Applied Materials Interfaces. **2022**, 14, 43508–43516.

[28] Fan, R. Y.; Zhao, H. Y.; Zhen, Y.-N.; Wang, F.-G.; Hu, H.; Chai, Y.-M.; Dong, B. Mn-Induced Strengthening Hybridization Effect of Co–O Bond for Stable Oxygen Evolution in Acidic Media. Fuel. **2023**, 333, 126361.

[29] Guan, X.; Sun, X.; Feng, H.; Zhang, J.; Wen, H.; Tian, W.; Zheng, D.; Yao, Y. Rational Interface Engineering of Cu_2S–CoO_x/CF Enhances Oxygen Evolution Reaction Activity. Chemical Communications. **2020**, 56, 13571–13574.

[30] Farid, S.; Qiu, W.; Zhao, J.; Song, X.; Mao, Q.; Ren, S.; Hao, C. Improved OER Performance of Co_3O_4/N-CNTs Derived from Newly Designed ZIF-67/PPy NTs Composite. Journal of Electroanalytical Chemistry. **2020**, 858, 113768.

[31] Abdalla, I.; Shen, J.; Yu, J.; Li, Z.; Ding, B. Co_3O_4/Carbon Composite Nanofibrous Membrane Enabled High-Efficiency Electromagnetic Wave Absorption. *J. Scientific Reports* **2018**, *8* (1).

[32] Qin, Z.; Wang, C.; Ma, Y.; Xia, L.; Zhong, B.; Li, X.; Zhang, P. ZIF-67/GNs Derived Co_3O_4/GNs Multilayer Flower and Porous Structure as an Efficient Electromagnetic Wave Absorbing Material for Excellent Absorbing Properties. *J. Applied Surface Science* **2022**, *575*, 151789.

[33] Gu, W.; Quan, B.; Liang, X.; Liu, W.; Ji, G.; Du, Y. Composition and Structure Design of Co_3 O_4 Nanowires Network by Nickel Foam with Effective Electromagnetic Performance in C and X Band. *J. ACS Sustainable Chem. Eng.* **2019**, *7* (5), 5543–5552.

[34] Yusuf, J. Y.; Soleimani, H.; Noorhana Yahya; Sanusi, Y. K.; Adebayo, L. L.; Sikiru, S.; Wahaab, F. A. Recent Advances and Prospect of Cobalt Based Microwave Absorbing Materials. *J. Ceramics International* **2020**, *46* (17), 26466–26485.

[35] Liu, T.; Zhou, P. H.; Xie, J. L.; Deng, L. J. The Hierarchical Architecture Effect on the Microwave Absorption Properties of Cobalt Composites. *J. Journal of Applied Physics* **2011**, *110* (3).

[36] Li, J.; Zhao, X.; Liu, J.; Zhang, L.; Yang, C. Ultralight Carbon-Based $Co(OH)_2$-Co_3O_4/ Nanocomposite with Superior Performance in Wave Absorption. *J. Journal of Alloys and Compounds* **2019**, *777*, 954–962.

[37] Liu, T.; Pang, Y.; Zhu, M.; Kobayashi, S. Microporous co@CoO Nanoparticles with Superior Microwave Absorption Properties†. *J. Nanoscale* **2014**, *6* (4), 2447.

[38] Liu, Y.; Zhang, Z.; Xiao, S.; Qiang, C.; Tian, L.; Xu, J. Preparation and Properties of Cobalt Oxides Coated Carbon Fibers as Microwave-Absorbing Materials. *J. Applied Surface Science* **2011**, *257* (17), 7678–7683.

[39] Chen, H.; Hong, R.; Liu, Q.; Li, S.; Huang, F.; Lu, Y.; Wang, L.; Li, K.; Zhang, H. CNFs@carbonaceous Co/CoO Composite Derived from CNFs Penetrated through ZIF-67 for High-Efficient Electromagnetic Wave Absorption Material. *J. Journal of Alloys and Compounds* **2018**, *752*, 115–122.

[40] Wang, X.; Zhou, P.; Qiu, G.; Zhang, X.; Wang, L.; Zhang, Q.; Wang, M.; Liu, Z. Excellent Electromagnetic Wave Absorption Properties of Porous Core-Shell CoO/co@C Nanocomposites Derived from a Needle-Shaped $Co(OH)_2$@ZIF-67 Template. *J. Journal of Alloys and Compounds* **2020**, *842*, 155807.